Barometer-based Tactile Skin for Anthropomorphic Robot Hand

Risto Kõiva*, Tobias Schwank, Guillaume Walck, Martin Meier, Robert Haschke and Helge Ritter

Abstract— We present our second generation tactile sensor for the Shadow Dexterous Hand's palm. We were able to significantly improve the tactile sensor characteristics by utilizing our latest barometer-based tactile sensing technology with linear ($R^2 \geq 0.9996$) sensor output and no noticeable hysteresis. The sensitivity threshold of the tactile cells and the spatial density were both dramatically increased. We demonstrate the benefits of the new sensor by re-running an experiment to estimate the stiffness of different objects that we originally used to test our first generation palm sensor. The results underline a considerable performance boost in estimation accuracy, just due to the improved tactile skin. We also propose a revised neural network architecture that even further improves the average classification accuracy to 96% in a 5-fold cross-validation.

I. INTRODUCTION

Equipping robotic hands with advanced tactile sensing capabilities, along with a fundamental understanding of motor-control processes, will eventually lead to universal dexterous robots capable of executing manual everyday activity tasks [1] that require a high degree of manual intelligence [2], comparable to the level seen in humans. We have previously developed tactile sensors for the fingertips [3], [4] and palms [5] of robotic hands – areas containing the highest density of mechanoreceptors in human hands [6]. The present work was motivated by our robotics grasping and manipulation experiments, revealing the necessity to improve the spatial resolution and the sensor sensitivity of our previous palm sensor [5].

Covering palms of robotic hands with sensors has been pursued before [7]–[13], but to the best of our knowledge, no other research group has tried to tackle adding tactile sensing to such a complex and curved robotic palm shape as the one of the Shadow Dexterous Robot Hand (SDRH) [14]. Although the present work explicitly targets SDRH, the underlying technology is applicable to a wide variety of robotic hands.

In the present work we were able to significantly improve on our previous palm sensor for the SDRH [5], by considerably increasing the sensitivity and the spatial density of the tactile cells. Our newly developed barometer-based tactile sensors have a linear characteristic and show no noticeable hysteresis. Sec. II discusses the details of the construction. Sec. III presents the results of the evaluation of the novel barometer-based sensing technology. In Sec. IV, we present
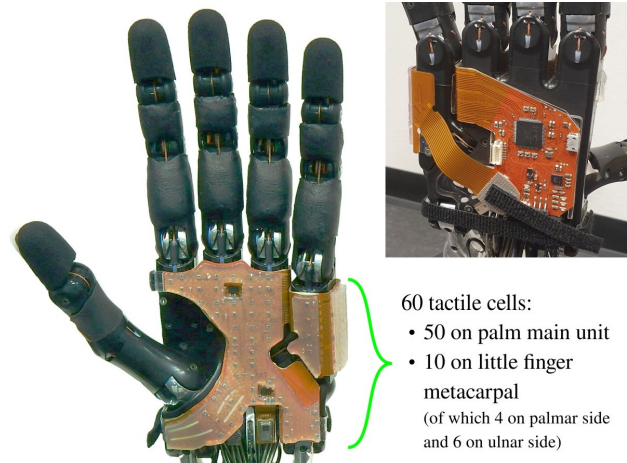
Fig. 1. Our 2nd gen. palm tactile sensor for the Shadow Dexterous Hand. 54 tactile cells cover the palmar surface (of which 50 are on the main unit and 4 on the little finger unit) and additional 6 cells cover the ulnar side of the little finger metacarpal. The upper right inset shows the dorsal side of the sensor with a flexible attachment of the little finger unit, a power distributing circuitry, external communication ports, and a microcontroller.

an improved neural network architecture that extends our earlier work [5], along with a re-run of the old architecture on the novel sensor to systematically assess the benefits of the novel sensor design, and, separately, its potential when connected with a richer neural network architecture. We conclude with a discussion and present ideas of future work in Sec. V.

II. DETAILS OF CONSTRUCTION

We set out to create an upgraded palm sensor for the SDRH, with the main goal to improve on tactile sensing by increasing contact sensitivity and spatial density. Fig. 1 presents the final sensor, mounted onto a left SDRH.

A. Tactile sensing

Tactile sensors based on various transduction principles have been developed in the past [15]–[17], whereas in the present work we identified MEMS-based barometer sensors as one promising solution towards robust high-resolution tactile sensing and invested effort into its further development.

The barometer-based tactile sensing was pioneered in Robert Howe's lab at Harvard University by Jentoft and Tenzer [18], [19] and commercialized as TakkTile [20]. As sensing elements, they used MPL115A digital barometer chips by NXP Semiconductors, cast in rubber. The rubber layer transmitted the external contact forces onto the MEMS membrane inside the barometer chip. The MPL115A has, in today's view, a relatively thick package with a height of 1.2 mm and a printed circuit board (PCB) footprint of 15
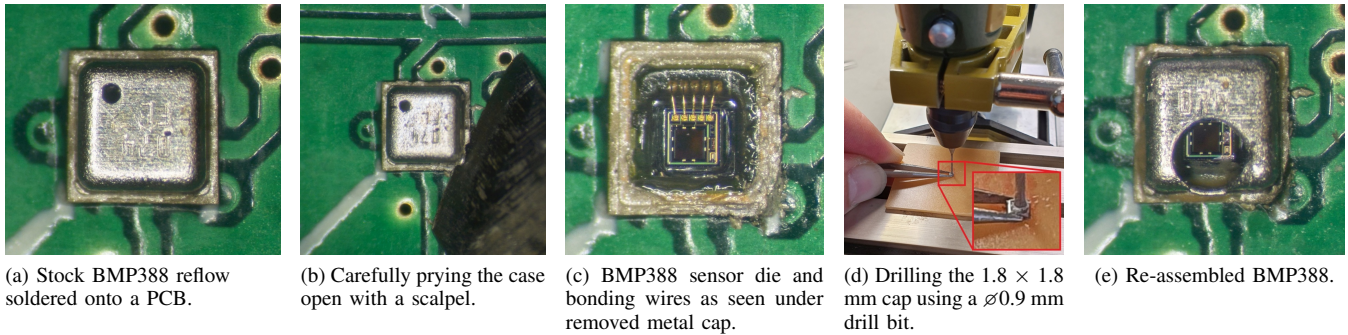
(a) Stock BMP388 reflow soldered onto a PCB.

(b) Carefully prying the case open with a scalpel.

(c) BMP388 sensor die and bonding wires as seen under removed metal cap.

(d) Drilling the 1.8 × 1.8 mm cap using a ⌀0.9 mm drill bit.

(e) Re-assembled BMP388.

Fig. 2. The modification steps to enlarge the orifice of a BMP388 digital barometer chip from factory ⌀0.25 mm to ⌀0.9 mm. **(a)** The chip is soldered onto a PCB for easier handling. **(b)** The cap is carefully removed using a scalpel, revealing the sensor die and its bonding wires **(c)**. **(d)** With tweezers, the cap is positioned and held steady during drilling. **(e)** The modified cap is re-glued, but rotated 180° relative to the original orientation. This hides and protects the bonding wires under the cap from physical damage.

mm^2, without counting the required peripheral components. As we planned our sensor as an add-on attachment to the SDRH, it was important for us to create the palm sensor as thin as possible in order not to limit the movement of the joints and grasping range of the SDRH. Our search for a smaller and higher resolution alternative to MPL115A with only 10-bit output quickly revealed one significant property, all newer and smaller barometer chips were missing, namely an orifice big enough to allow the silicone rubber to easily reach the MEMS membrane when cast in a vacuum chamber. Newer and smaller MEMS barometer chips, such as ST Microelectronics LPS22HD and LPS35HW, Amphenol Advanced Sensors NPA201, TE Connectivity MS5637 or Bosch Sensortec BMP388/390, come with orifice sizes of only ⌀20 µm to ⌀0.4 mm. An orifice in this size prevents the silicone rubber from reaching the MEMS layer using previous manufacturing techniques, resulting in strong signal drift and hysteresis due to an air gap remaining between the MEMS layer and the silicone, as shown in Sec. III or in [21].

After identifying the reason for the mediocre performance of tactile sensors based on such tiny MEMS barometer chips, we looked for a way to enlarge the ⌀0.25 mm orifice of the Bosch-Sensortec BMP388, the smallest digital barometer chip known to us currently available on the market, with a package size of only 2.0×2.0×0.75 mm. Simply enlarging the hole in the metal cap by drilling, usually damaged the chips. Also, removing the cap completely and directly casting the chips in silicone rubber was not successful, as without the protective cap, the delicate bonding wires easily got damaged under stronger interaction forces. But we were successful by dismantling the cap, drilling and deburring a bigger hole and mounting the cap back onto its base with the MEMS die.

We begin the modification by soldering the BMP388 sensor chips onto a PCB for fixation (Fig. 2a). The next step is the most delicate one: using a scalpel, we carefully pry the case open (Fig. 2b), while avoiding contact with the sensor die and the bonding wires (Fig. 2c). The scalpel is pressed solely into the corners opposite of the bonding wires. Fig. 2c displays the sensor where the cap has been successfully removed, revealing the die and the bonding wires. The proper operation of the chip is checked with a microcontroller-based readout circuit at this stage. In the next step, the removed cap is modified using a ⌀0.9 mm drill bit, while it is positioned and held in place with tweezers (Fig. 2d). After drilling, the cap is carefully deburred and cleaned, before it is glued back onto the sensor using Loctite 3612 epoxy surface mount adhesive. The cap is rotated by 180° relative to the original factory configuration in order to position the orifice as close as possible over the MEMS membrane and at the same time as far away as possible from the bonding wires in order to shield them best from mechanical stresses occurring later during usage as a tactile sensor cell. The glue is hardened roughly for 3 minutes inside an oven heated to ≈150°C. Fig. 2e displays the re-assembled BMP388.

B. Sensor shape and construction

To fit the shape of the SDRH, we modeled a flex-PCB around the 3D shape of the palm employing the sheet metal environment of the Solid Edge CAD software and used its *flatten* function to retrieve the required 2D contour (Fig. 3). Using this contour, we designed a double-layered flex-PCB, applying all common design rules [22].

Due to the elevated effort to manually enhance a single barometer sensor (taking roughly 15 min per sensor), we limited the overall amount of sensors to 60, which we distributed uniformly on a 6×8 mm grid across the palmar side of the hand. In principle, due to the small package size of the sensor, a spatial resolution of up to 2.2 mm is possible as

Fig. 3. From 3D shape to flat shape contour to be used as a guide for developing the flexible PCB, the base of the palm sensor. **(left)** The 3D model of the sensor shape is constructed in CAD to cover the palm. **(middle)** The sensor shape in 3D without SDRH. **(right)** Flattened shape of the sensor. (For simplicity, middle and right images do not show the little finger metacarpal unit)
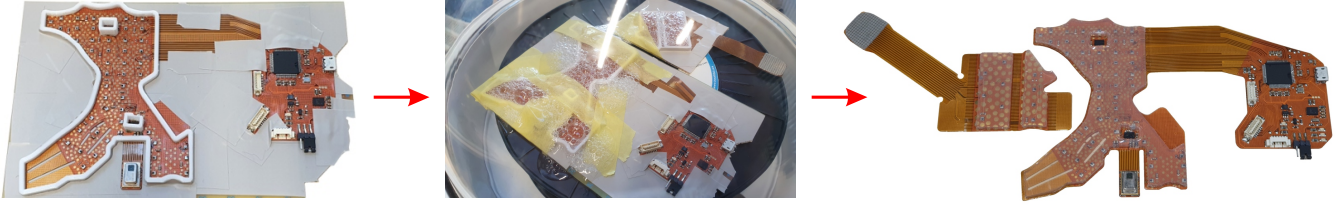
Fig. 4. Casting the silicone rubber. **(left)** Plastic frames help to contain the silicone only in desired areas. **(middle)** De-gassing the silicone rubber in a vacuum chamber after casting. **(right)** The palm sensor with a 3 mm thick rubber layer after degassing and silicone drying, ready to be mounted onto robotic hand.

we have demonstrated in a small 5×5 array [23]. For casting the sensor, we followed mostly the process described in [19], with some alterations that we describe next.

After cleaning the flex-PCB from the solder residue, we treated the flex-PCB areas surrounding the chips with a primer *MM4* from SilikonFabrik.de to improve adhesion of the silicone. Next, we placed a 3 mm high 3D-printed cast frame around the sensors (shown in white in Fig. 4 left image) and poured the silicone into the mold. To this end, a 2-component, room-temperature curable silicone, type *SF13*, was used (also from SilikonFabrik.de), resulting in a shore hardness of 13 ShA. Next, we evacuated the entrained air bubbles in a vacuum chamber at 200 mbar for 15 minutes (Fig. 4 middle). As still some bubbles remained after this process, we increased the vacuum to 50 mbar and continued the process for additional 5 minutes. After bringing the sensor back to atmospheric pressure, it took roughly an hour for the remaining bubbles to disappear. The sensor was given an additional whole day to fully cure at room temperature and atmospheric pressure, before the cast frame was eventually removed (Fig. 4 right).

The BMP388 sensor chips are sampled via SPI bus at 100 Hz by a PIC32MZ microcontroller and the sampled data is currently relayed via USB-CDC to the controlling PC. The palm sensor is already prepared for optical pre-touch sensing, thermal imaging, motion and acceleration sensing and direct data transmission via SPI to the SDRH's data bus. The final integration of these components is future work. Within the present paper we only focus on tactile sensing.

III. EVALUATION

In order to evaluate the performance of the enhanced tactile sensor and compare it with an unmodified BMP388 chip, we designed a small test PCB with 4 tactile cells, using two stock and two enhanced barometer chips (Fig. 5).

First, we evaluated the sensor's temperature stability over time. To this end, we exposed the sensor test unit and a temperature reference sensor (Bosch Sensortec BMP280) to the sun on a cloudy day and recorded the sensor output, including the temperature, over the course of roughly 2 hours. Fig. 6 plots the corresponding data. The red curve displays the temperature fluctuation within a range of roughly 3°C over the course of the experiment. Note, that the *raw* sensor values decrease with increasing pressure. To facilitate comprehension, we have inverted the raw sensor axis in this and all upcoming figures. Interestingly, both unmodified
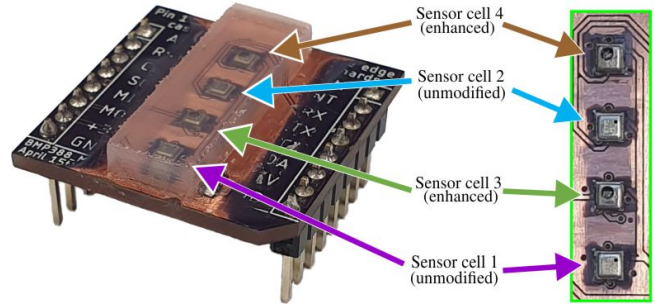

Fig. 5. BMP388-based tactile sensor test unit with four cells. Interleaved, two stock and two enhanced BMP388 digital barometer chips (with enlarged orifices) are populated. The right image shows the chips before casting in silicone rubber for improved visibility.
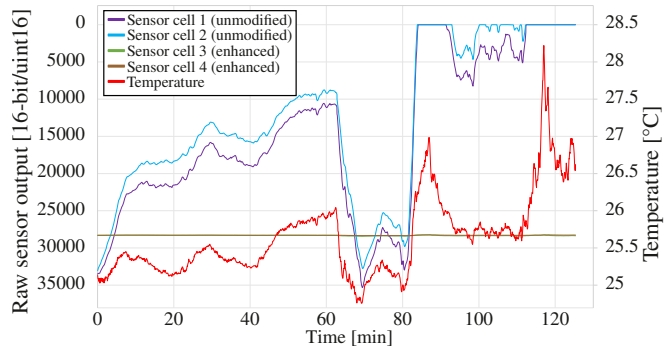

Fig. 6. Temperature dependency of two unmodified stock and two enhanced tactile sensor cells while exposed to the sun for 2 hours. The cells with unmodified chips (blue and purple curves) show high, but undesired, correlation to the temperature (red), whereas the enhanced cells (brown and green curves) show almost no dependency on temperature. Their curves overlap, resulting in a single green-brown line only.

BMP388 chips (blue and purple curves indicating their raw pressure sensor output) show a strong, but undesired correlation to temperature, whereas the enhanced sensor cells (shown in green and brown) are stable and independent from temperature. Please note that the graphs of the enhanced cells mostly overlap, while the stock sensors exhibit slightly different behavior – due to different volumes of air enclosed between their MEMS layer and the silicone.

In the second evaluation, we looked at the sensor performance, while repeatedly applying a triangular force pattern from 0 to 3 N and back. 3 N was previously experimentally found to be meaningful limit, slightly above the saturation point of our enhanced sensor cells. For applying the force, we used a custom-built measurement rig with a calibrated, industrial force sensor (ME-Meßsysteme GmbH KD45 ±10N,
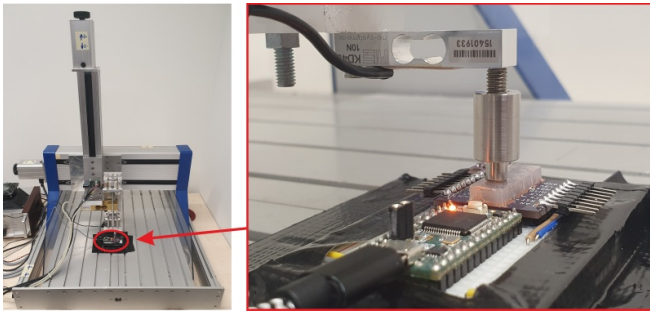
Fig. 7. Custom built measurement rig with a calibrated industrial strain gauge reference sensor mounted on a numerically controlled linear axis. The close-up shows the reference sensor with the probe tip and our test unit with four BMP388 sensors next to the readout electronics.

Fig. 9. Sensor signals of Fig. 8 plotted as raw sensor output vs. reference force. The enhanced sensors (in green and brown) show a slight manufacturing difference, but overall very similar performance with almost no hysteresis or noise, and perfect linearity (R^2=0.9996 and 0.9998 resp.). In contrast, the behavior of the unmodified sensor cells strongly differs: sensor 2 (blue) exhibits strong variance between trials, while sensor 1 (purple) is rather insensitive within the 3 N force range.

accuracy class 0.1%) for ground-truth reference (Fig. 7). The reference sensor was moved on a vertical linear axis by a stepper motor. The signal was sampled using a data acquisition card with 16-bit ADC. The linear movement was transformed into a force via a spring between the axis and the reference sensor. For our tests, we used a cylindrical ∅5 mm probe tip. Fig. 7 right shows a close-up of the reference sensor, the probe tip, our test sensor with four BMP388 chips and the readout electronics.

After each movement step of the rig a pause of 1 s was kept for the mechanics to stabilize before a new measurement was taken. The triangular force profile was applied 5 times, before the probe was advanced to the next tactile cell. Each cycle lasted ≈4.5 minutes resulting in a total duration of 1.5 hours. The resulting output of all 20 trials is depicted in Fig. 8. Fig. 9 plots the same data as the sensor characteristic of all 4 sensor cells. The enhanced sensors (shown in green and brown) display low variance in performance, whereas the unmodified sensor cells (shown in blue and purple) exhibit significant variance between the cells. Our enhanced cells show superior, almost linear ($R^2 \geq 0.9996$) characteristic without noticeable hysteresis, whereas the unmodified cells show high variance between single trials and between the cells as well. As can be taken from Fig. 9, the modified sensors cover a force range of 2.8 N, which – given the small probe tip – corresponds to a pressure of ≈ 140 kPa.

A small saturation can be noticed for both modified sensors close to the maximum force of 3 N, while the unmodified sensors either saturate much earlier (#2) or later (#1).

Our third experiment investigated the sensitivity threshold of the sensors. To this end, we applied precision weights in 10 mg steps onto the modified sensor cells and observed the raw sensor value. As soon as this changed, we noted the value. We tested both of our enhanced cells 10 times and found 20 mg to be the reliable detection threshold. With a weight ∅5 mm, this evaluates to a sensitivity threshold pressure of just ≈ 10 Pa. In comparison, even a 10 g weight on top of the unmodified cells was not enough for a reliable detection threshold due to strong drift of the sensor output.

These results show that our tactile sensor cells, based on enlarged-orifice BMP388 barometer chips, not only outperform our previous palm sensor [5], but exhibit a significant performance boost also when compared to the original MPL115A-based tactile sensors [13], [18], [19].

Fig. 10 illustrates the tactile skin activation when holding various objects – employing our ROS tactile toolbox [24] for visualization. The 4 image pairs each show the held object and the visualization of tactile responses in `RViz`, in which object-specific contact patterns can be easily observed.
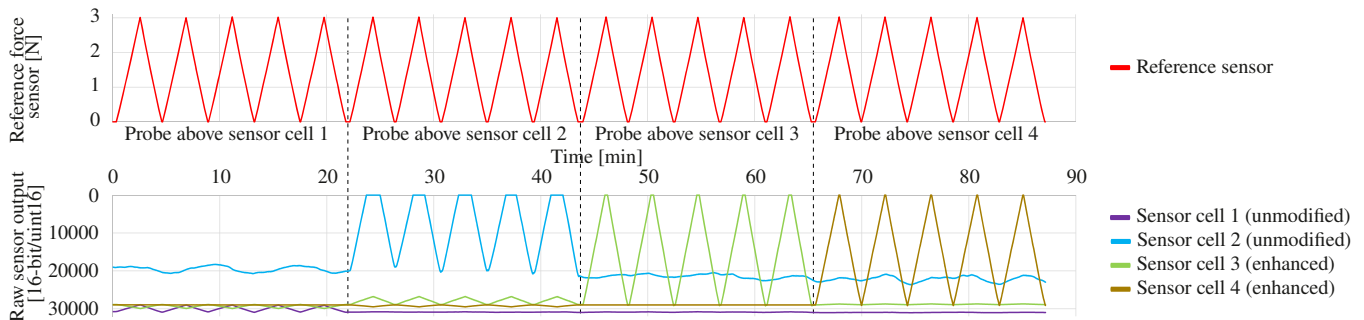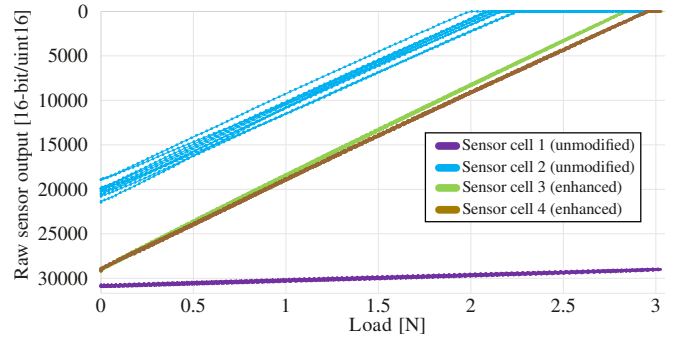

Fig. 8. Evolution of the sensor signals while applying triangular force profiles to the 4 sensor cells of the test unit shown in Fig. 5. The top diagram shows the reference force and the bottom diagram displays the raw sensor outputs. Ideally, a sensor's signal should exactly follow the reference force in exactly one segment (when it is probed). While the enhanced cells exactly follow the signal (and even slightly react to the probing of neighboring cells), the unmodified sensors are rather unresponsive (sensor 1) or noisy (sensor 2). Also, the unmodified sensors exhibit very different sensitivity.

(a) Allen key (170 g)   (b) Bottled water (314 g)   (c) Ball bearing (102 g)   (d) Marble (4 g)   (e) Colormap
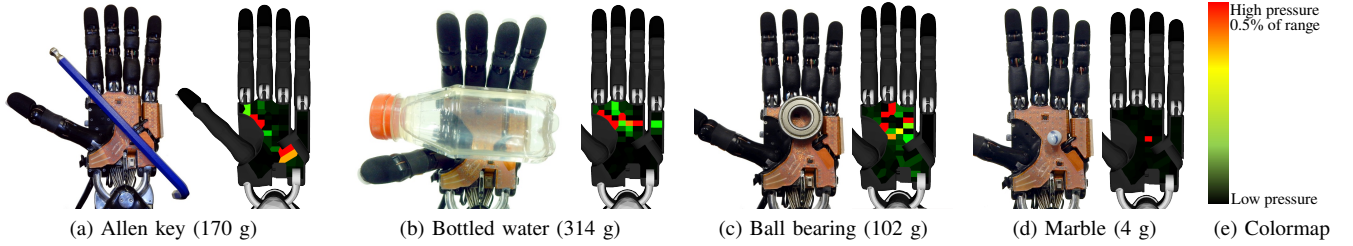
Fig. 10. Visualized tactile sensor output when touching objects with features. The output is color-coded from dark green for low pressure, over green and yellow to red denoting pressure at 0.5 % of the range (ca. 700 Pa). The contact area and force profile can be clearly observed in the sensor output visualization.
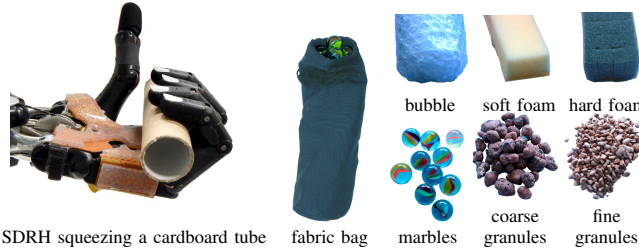

SDRH squeezing a cardboard tube   fabric bag   bubble   soft foam   hard foam   marbles   coarse granules   fine granules

Fig. 11. Leftmost image shows an experiment trial in progress. To the right are the other test objects: bags fitted with different materials.
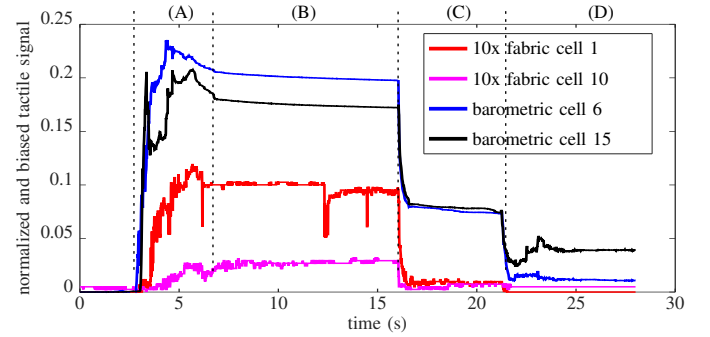

Fig. 12. Example tactile signals of 2 active cells for the fabric-based (red, magenta) and the barometer-based (black and blue) sensor, during the 4 phases (A to D) when squeezing a bag of coarse granules. Signals were normalized, biased, and resized (x10 for fabric sensors). Even despite this resizing, the barometer sensors exhibit a much stronger signal.

IV. APPLICATION: STIFFNESS ESTIMATION

An important task in everyday activities which requires a sensitive sense of touch is the handling of soft objects like food. We evaluate the barometric sensor in a stiffness classification task and compare its performance to our previous, fabrics-based palm sensor with the same settings as in [5] and an additional, improved neural network architecture.

The experiment consisted of squeezing 7 cylindrical objects against the palm with all 4 fingers. The considered objects are shown in Fig. 11. Recorded sensors include palm and fingertip [3] tactile sensors as well as joint angles.

To avoid learning the material solely from the size of the bag (i.e. employing the hand posture), their initial diameter is very similar across all objects (4 − 5.5 cm). An experiment trial is decomposed into 4 phases: A) squeezing the object, B) maintaining the grasp posture for 10 s, C) relaxing the tendons for 5 s, and D) actively opening the hand. To obtain a dataset for training, we performed ten trials for each of the 7 objects. Note that a force-limiting algorithm [25] runs to protect the hand's tendons in phases A and B, which resulted in a slight decay of the grasping force over time. For more details about the original experiment, please refer to [5].

Fig. 12 compares some typical signals of the old and new palm tactile sensors when squeezing a bag of coarse granules. All signals were normalized to their respective ADC ranges and biased to start at zero. The new sensor exhibits an almost 20 times larger signal amplitude compared to the older, fabric-based one, which operates close to the ADC resolution. Moreover, the new sensor provides higher ADC resolution and is less noisy during the motionless phases.

We classified the obtained sensor sequences with a recurrent neural network, composed of several LSTM nodes [26]. An LSTM node can efficiently memorize context over time and thus learn long-time dependencies within the input

signal. In our case, the network needs to extract the object stiffness from the time-evolution of the force profile with respect to the finger-closing trajectory. A stronger force increase while closing the fingers is correlated to a higher stiffness. Each LSTM node has a central recurrent unit, which has gated, recurrent connections to the input and output layers as well as to all other LSTM nodes within a layer. Additionally, each node has a forget gate, which allows the node to reset its state upon specific input events. Formally, the core update equations of a single LSTM node c at time t are given as:

$$c_t = g_t^f \otimes c_{t-1} + g_t^{in} \otimes \sigma(W_c x_t + R_c h_{t-1} + b_c) \quad (1)$$
$$h_t = g_t^{out} \sigma(c_t), \quad (2)$$

with trainable weight matrices W_c and R_c for input and recurrent connections, and a trainable bias term b_c. x_t is the input, h_t the internal state, and c_t the context at time t. The gating functions $g^{\{in,f,out\}}$ are implemented as standard neurons:

$$g_t^* = \sigma^*(W_* x_t + R_* h_{t-1} + b_*) \quad (3)$$

with gate-specific, trainable weights W_*, R_* and biases b_*. The nonlinear activation function σ typically is the tanh.

As can be seen in Fig. 12, a typical squeezing sequence lasted $\approx$14 s. We fed the network with temporal sensor sequences comprising the phases A and B only, i.e. squeezing and holding. The sequence start was automatically extracted from the tactile fingertip recordings using a small touch threshold (2% of the tip's sensor range) to detect the first contact of a finger squeezing the object. The end of the

#	sensor data	network	accuracy
1	fabric palm, old rec. [5]	12-160-7	57.77%
2	(1) + finger tips + joints	36-240-7	77.57%
3	fabric palm, new rec.	12-160-7	$54.07 \pm 4.37\%$
4	barometer palm	60-160-7	$80.96 \pm 2.79\%$
5	fabric palm, new rec.	12-160-128-64-7	$63.35 \pm 3.31\%$
6	barometer palm	60-160-128-64-7	$91.17 \pm 1.12\%$
7	(6) + finger tips + joints	84-160-128-64-7	$\mathbf{96.62 \pm 1.07\%}$
	random chance		14.28%

TABLE I

RECURRENT NETWORK CLASSIFICATION RESULTS.

sequence was defined by the trigger signal to relax tendons. The input sequences were split into slices of 500 ms, which were used to train the network in batches. Given a sampling frequency of 100 Hz, a slice comprised 50 samples. For 5-fold cross-validation, the set of batches was split into five equally sized subsets.

We first trained on the same architecture as in [5], which consisted of n sensor inputs, a hidden-layer of 160 LSTM nodes, and 7 soft-max output units encoding the probability of the 7 different objects. The network was trained with stochastic gradient descent (SGD) as optimizer for 50 epochs, as in [5]. The resulting prediction accuracies obtained from cross-validation are shown with their mean and standard deviation in the upper part of Table I. We assured that each of the seven classes contains the same number of samples, so the accuracy in this case is defined as the ratio of the number of correctly classified samples wrt. all samples. For the fabric-based sensor, the results are close to the ones obtained in the original experiment [5]. The new recordings (row 3) yield slightly worse results than the original ones (row 1) due to the wear of the sensors over the past five years. The barometer sensors (row 4) yield results in the range of 80%, which we could achieve in [5] only by combining the palm sensors with the more sensitive fingertip sensors as well as finger flexion joints.

We additionally explored deeper network architectures and employed the more recent Adam optimizer [27], now for 100 epochs. The best network performance was achieved by augmenting the original network with two additional hidden layers comprising 128 and 64 units with ReLu activation. These new results are shown in the lower half of Table I. The supplementary video demonstrates the sensor in action.

V. CONCLUSION & FUTURE WORK

We presented a barometer-based tactile skin for the Shadow Dexterous Hand, exhibiting significant performance improvements compared to our previous palm sensor. The new tactile skin provides higher sensitivity, higher signal and spatial resolution, has superb linearity and experiences almost no hysteresis. We were able to clearly demonstrate the superior performance of the sensor in a realistic robotic experiment of estimating the stiffness of objects.

Our next steps will be to fully integrate and exploit the other sensors (pre-touch, thermal imaging, IMU) for novel robotic manipulation applications. We are also planning to integrate the data transmission with the hand's internal SPI-to-EtherCAT bus to get rid of the external USB connection.

REFERENCES

[1] M. Beetz, M. Tenorth, and J. Winkler, "Open-EASE – A Knowledge Processing Service for Robots and Robotics/AI Researchers," in *ICRA*. IEEE, 2015, pp. 1983–1990.
[2] H. J. Ritter, R. Haschke, and J. J. Steil, "A Dual Interaction Perspective for Robot Cognition: Grasping as a "Rosetta Stone"," in *Perspectives of Neural-Symbolic Integration*, ser. Studies in Computational Intelligence. Springer Berlin / Heidelberg, 2007, vol. 77, pp. 159–178.
[3] R. Kõiva, M. Zenker, C. Schürmann, R. Haschke, and H. J. Ritter, "A highly sensitive 3D-shaped tactile sensor," in *Proc. AIM*, 2013.
[4] R. Kõiva, T. Schwank, G. Walck, R. Haschke, and H. J. Ritter, "Mechatronic fingernail with static and dynamic force sensing," in *IROS*, 2018, pp. 2114–2119.
[5] G. Büscher, M. Meier, G. Walck, R. Haschke, and H. J. Ritter, "Augmenting curved robot surfaces with soft tactile skin," in *IROS*, 2015, pp. 1514–1519.
[6] R. S. Johansson and J. R. Flanagan, "Coding and use of tactile signals from the fingertips in object manipulation tasks," *Nature reviews. Neuroscience*, vol. 10, pp. 345–359, 2009.
[7] T. Mouri, H. Kawasaki, K. Yoshikawa, J. Takai, and S. Ito, "Anthropomorphic Robot Hand : Gifu Hand III," *ICCAS*, 2002.
[8] H. Hasegawa, Y. Mizoguchi, K. Tadakuma, A. Ming, M. Ishikawa, and M. Shimojo, "Development of intelligent robot hand using proximity, contact and slip sensing," in *ICRA*, 2010, pp. 777–784.
[9] A. Schmitz, M. Maggiali, L. Natale, and G. Metta, "Touch sensors for humanoid hands," in *RO-MAN*, 2010, pp. 691–697.
[10] E.-H. Kim, S.-W. Lee, and Y.-K. Lee, "A dexterous robot hand with a bio-mimetic mechanism," *International Journal of Precision Engineering and Manufacturing*, vol. 12, no. 2, pp. 227–235, 2011.
[11] J. Schill, J. Laaksonen, M. Przybylski, V. Kyrki, T. Asfour, and R. Dillmann, "Learning continuous grasp stability for a humanoid robot hand based on tactile sensing," in *BioRob*, 2012, pp. 1901–1906.
[12] S. Ye, K. Suzuki, Y. Suzuki, M. Ishikawa, and M. Shimojo, "Robust robotic grasping using IR Net-Structure Proximity Sensor to handle objects with unknown position and attitude," in *Proc. ICRA*, 2013.
[13] L. U. Odhner, L. P. Jentoft, M. R. Claffee, N. Corson, Y. Tenzer, R. R. Ma, M. Buehler, R. Kohout, R. D. Howe, and A. M. Dollar, "A compliant, underactuated hand for robust manipulation," *The International Journal of Robotics Research*, vol. 33, no. 5, pp. 736–752, 2014.
[14] "Shadow Dexterous Hand, Shadow Robot Company," http://www.shadowrobot.com/products/dexterous-hand/.
[15] R. S. Dahiya, G. Metta, M. Valle, and G. Sandini, "Tactile Sensing—From Humans to Humanoids," *IEEE Transactions on Robotics*, vol. 26, no. 1, pp. 1–20, 2010.
[16] Z. Kappassov, J.-A. Corrales, and V. Perdereau, "Tactile sensing in dexterous robot hands — Review," *Robotics and Autonomous Systems*, vol. 74, pp. 195 – 220, 2016.
[17] L. Zou, C. Ge, Z. J. Wang, E. Cretu, and X. Li, "Novel Tactile Sensor Technology and Smart Tactile Sensing Systems: A Review," *Sensors*, vol. 17, no. 11, 2017.
[18] L. P. Jentoft, Y. Tenzer, D. Vogt, Jia Liu, R. J. Wood, and R. D. Howe, "Flexible, stretchable tactile arrays from MEMS barometers," in *ICAR*, 2013, pp. 1–6.
[19] Y. Tenzer, L. P. Jentoft, and R. D. Howe, "The Feel of MEMS Barometers: Inexpensive and Easily Customized Tactile Array Sensors," *IEEE Robotics Automation Magazine*, vol. 21, no. 3, pp. 89–95, 2014.
[20] "TakkTile sensors, RightHand Robotics Inc." https://www.labs.righthandrobotics.com/takktile-sensors.
[21] P. Weiner, C. Neef, and T. Asfour, "A Multimodal Embedded Sensor System for Scalable Robotic and Prosthetic Fingers," in *Humanoids*, 2018, pp. 286–292.
[22] "Design-Rules for Flex- or Rigid-Flex circuit boards," https://www.multi-circuit-boards.eu/en/pcb-design-aid/flex-rigid-flex.html.
[23] R. Kõiva, T. Schwank, R. Haschke, and H. J. Ritter, "Towards high-density barometer-based tactile sensor arrays," in *RoboTac Workshop at IROS*, 2019.
[24] Tactile toolbox: https://github.com/ubi-agni/tactile_toolbox.
[25] G. Walck, R. Haschke, M. Meier, and H. J. Ritter, "Robot self-protection by virtual actuator fatigue: Application to tendon-driven dexterous hands during grasping," in *IROS*, 2017, pp. 2200–2205.
[26] S. Hochreiter and J. Schmidhuber, "Long short-term memory," *Neural Computation*, vol. 9, no. 8, pp. 1735–1780, 1997.
[27] D. P. Kingma and J. Ba, "Adam: A method for stochastic optimization," *arXiv preprint arXiv:1412.6980*, 2014.